MDPI

Article

Flue Gas Desulfurization in a Fixed-Bed Reactor: Mild-Condition Uptake Through Different Adsorbent Materials

Maura Mancinelli [1],*,[†] , Elena Spagnoli [1],*,[†] , Francesco Di Benedetto [1] , Vito Cristino [2] , Matteo Valt [3] , Giordano Montegrossi [4] , Luca Barion [1] , Lia Vanzetti [3] , Andrea Gaiardo [3] , Gabriele Vola [5] , Mattia Massa [6] , Annalisa Martucci [1] , Sandro Gherardi [1] and Matteo Ardit [7]

[1] Department of Physics and Earth Sciences, University of Ferrara, 44122 Ferrara, Italy; francesco.dibenedetto@unife.it (F.D.B.); luca.barion@unife.it (L.B.); mrs@unife.it (A.M.); gherardi@fe.infn.it (S.G.)
[2] Department of Chemical, Pharmaceutical and Agricultural Sciences, University of Ferrara, 44122 Ferrara, Italy; vito.cristino@unife.it
[3] Sensors and Devices Center, Bruno Kessler Foundation, 38123 Trento, Italy; mvalt@fbk.eu (M.V.); vanzetti@fbk.eu (L.V.); gaiardo@fbk.eu (A.G.)
[4] Institute of Geosciences and Georesources, IGG-CNR, 50121 Firenze, Italy; giordano.montegrossi@igg.cnr.it
[5] Cimprogetti Spa, The Green Edge of Lime Technologies, 24044 Dalmine, Italy; g.vola@cimprogetti.com
[6] INSTM and Chemistry for Technologies Laboratory, Department of Mechanical and Industrial Engineering, University of Brescia, via Branze 38, 25123 Brescia, Italy; mattia.massa@unibs.it
[7] Department of Geosciences, University of Padova, 35131 Padova, Italy; matteo.ardit@unipd.it
*   Correspondence: maura.mancinelli@unife.it (M.M.); elena.spagnoli@unife.it (E.S.)
[†] These authors contributed equally to this work.

Abstract: In quest of a substantial reduction in potentially toxic gas emissions into the air from industrial plants, dry flue gas desulfurization (FGD) systems offer several advantages, such as reduced operational costs, adaptability, ease of use, and the elimination of liquid waste. This study describes the development of a laboratory-scale pilot system for conducting SO_2 abatement experiments using a fixed-bed reactor. To validate the experimental setup, the reactor was equipped with a control system for measuring and monitoring relative humidity, temperature, and total flux composition. The study utilized two standards, slaked lime and 13X zeolite, under identical experimental conditions to ensure comparability. This research will significantly advance the understanding of adsorbent materials for capturing low SO_2 concentrations by measuring adsorption kinetics and equilibrium data. The findings highlight the impact of distinct morphological, chemical, and crystallographic properties on the efficiency of dry FGD systems.

Keywords: desulfurization; zeolite; portlandite; sulfur dioxide; FGD

1. Introduction

The imperative to reduce emissions of noxious gases has prompted extensive research into effective gas desulfurization methods, particularly in industrial settings where sulfur-containing compounds present significant environmental and health hazards [1–3]. Among the various sulfur-containing compounds, sulfur dioxide (SO_2) is of particular concern due to its toxicity and corrosive nature [3]. Efficient removal of SO_2 gas from industrial gas emissions is therefore a critical priority. SO_2 is a common byproduct of various industrial processes, including the combustion of fossil fuels and the manufacturing of cement, glass, paper, iron, steel, and copper. Consequently, sulfur dioxide emissions are strictly regulated by every industrialized nation on the planet [4]. The European Community (2016/2284/UE) outlined a plan to consistently reduce global SO_2 emissions, with the objective of reaching a 70% average decrease in SO_x across all Member States by 2030 [5]. For instance, for coal-fired power plants with a power generation capacity exceeding 300 MWth, the permitted SO_x content limit will be reduced to 200 ppm. Similar guidelines have been established

in the United States and China, where the limits for new plant installations are 350 and 90 ppm, respectively [5].

Flue gas desulfurization (FGD) technologies used to mitigate SO_2 emissions in flue gases can be classified into three principal categories: wet, semi-dry, and dry systems. The classification is based on the physical condition of the adsorbent and of the waste product, which can be in the form of liquid, slurry, or ash. Wet FGD systems, which employ liquid-phase adsorbents such as limestone solutions, have historically dominated the market due to their high efficiency, achieving SO_2 removal rates of 85–95%. However, SO_2 residual concentrations of up to 150–450 ppm can still result in significant emissions from conventional FGD systems, contributing to dozens of megatons of global anthropogenic SO_2 emissions annually from energy-related sources [6]. Furthermore, wet FGD technology sustainability is limited by high water consumption, low byproduct utilization rates, and the generation of secondary liquid waste [7]. Semi-dry FGD systems represent a cost-effective alternative, eliminating the need for reheating energy and wastewater treatment [8]. Since the 1980s, these systems have been commercially available, with the spray-drying process being the most suitable for the transformation of pre-existing power plants. Nevertheless, semi-dry systems are generally less efficient than wet systems [8]. For these reasons, it is expected that the global flue gas desulfurization market will experience the adoption of new strategies by leading players [9,10].

Among these, dry FGD systems are emerging as the market's fastest-growing technology [6]. Indeed, they offer several advantages, including lower operational costs, adaptability, ease of use, and the absence of liquid waste (which can be disposed of alongside fly ash) [6]. In comparison to other dry FGD systems, the dry fixed-bed FGD process facilitates straightforward testing of novel adsorbents. This process has already found industrial applications in two steel companies with SO_2 intake concentrations ranging from 250 to 800 ppm [11]. In one case, the temperature in the smelter off-gas was between 80 and 150 °C [11]. In addition to being proposed as an alternative treatment to wet FGD, the dry fixed-bed FGD can be suggested as a complement to the latter approach to entirely remove the exiting SO_2. In this scenario, the SO_2 concentrations arriving at the second FDG step would be modest, and the temperature of the flue gas would be lower than that utilized in the wet treatment, which is around 100–150 °C [12].

Research on dry FGD has predominantly focused on the SO_2 uptake capabilities of adsorbent materials under medium-to-high temperatures (150–850 °C) [13,14] and high SO_2 concentrations in the gas stream. Nevertheless, the FGD of some applications, such as those described above, operates in milder conditions, characterized by lower operating temperatures and SO_2 flux contents. Therefore, this work addressed this gap by developing a pilot system at laboratory scale, which was used to conduct SO_2 abatement experiments in mild conditions, including low reactor temperatures (T < 100 °C) and low SO_2 concentrations (600 ppm), with adsorbents located in a fixed-bed reactor. Moreover, relative humidity (RH%) was also considered, as increasing the RH% can improve the desulfurization efficiency of the system. The reactor modeling and data acquisition (DaQ) system, comprising humidity and temperature sensors, enabled comprehension of the experimental FGD conditions. Two known materials, namely, slaked lime ($Ca(OH)_2$) and 13X zeolite, were employed to validate the pilot dry fixed-bed FGD system in mild conditions. The experimental comparison and characterization of the SO_2 uptake performance of $Ca(OH)_2$ and the as-synthesized 13X zeolite, conducted under identical operational conditions, offer insights into the influence of distinct morphological, chemical, and crystallographic properties on FGD in mild conditions, namely, a low reactor temperature, SO_2 concentration, and RH%.

The findings will contribute to advancing the understanding of adsorbents for effective SO_2 capture, paving the way for more efficient gas desulfurization solutions in various industrial applications, particularly in the growing petrochemical sector. Indeed, in 2023, the global market for FGD systems was valued at over USD 4328 million and is expected to grow at a CAGR of around 6.8% by 2030 [9], with a notable shift toward more energy-

efficient and low-emission technologies [9,10]. This market growth will be accompanied by the development of next-generation systems, including dry and semi-dry FGD processes, which will offer improved flexibility, reduced operational costs, and lower environmental impacts compared to traditional wet FGD systems.

2. Materials and Methods

2.1. Choice of Adsorbent Materials

Two well-known adsorbent materials, slaked lime and 13X zeolite, were employed to validate the pilot dry fixed-bed FGD system in mild conditions.

Ca-based materials, namely, slaked lime ($Ca(OH)_2$), quicklime (CaO), limestone ($CaCO_3$), and calcium sulfide (CaS), are widely used as adsorbents in industrial FGD processes [15], despite some limitations. For instance, CaO requires hydration with water vapor to enhance its desulfurization capacity [15]. This preliminary treatment increases the operational costs of CaO and may lead to adsorbent inhomogeneity. $CaCO_3$ and CaS, on the other hand, emit pollutants and toxic gases, namely, CO_2 and S_2, respectively. In contrast, $Ca(OH)_2$ was chosen over the other industrial standards due to its strong basicity, which enables high reactivity vs. SO_2, especially in humid environments. Furthermore, the reaction of $Ca(OH)_2$ with SO_2 does not produce pollutant co-products, as evidenced in Equation (1) [15]:

$$Ca(OH)_2 + SO_2 + 1/2O_2 \rightarrow CaSO_4 + H_2O \tag{1}$$

Despite the advantages of $Ca(OH)_2$, including its low cost and abundance of raw material sources, several challenges remain to be addressed [15]. They include poor regeneration performances and lower sulfur uptake capacity than adsorbents with larger specific surface areas and better catalytic properties. These limitations have prompted exploration of innovative materials like transition metal oxide desulfurizers, activated carbons, mesoporous silica, metal–organic frameworks, and zeolites [16]. Among them, zeolites exhibit properties particularly well-suited to FGD applications [15], including high surface areas, good thermal stability, and promising regeneration potential [17].

Zeolite 13X (FAU-type topology) has already been proposed as an adsorbent for SO_2 due to its favorable catalytic properties, high surface area, and microporous structure. In 2017, Luo et al. [18] demonstrated that zeolite 13X, calcined at 500 °C in dry conditions, exhibits remarkable SO_2 adsorption characteristics. In 2018, Yang et al. [19] conducted a study on zeolite 13X, examining its adsorption capabilities for SO_2 and H_2S at high concentrations (>10,000 ppm) at a temperature of 150 °C and 15 vol % of water vapor. Moreover, 13X displayed good regeneration capabilities, which might be improved by the addition of reducing gases during the treatment [18]. The development of efficient regeneration processes would enable the economic and practical feasibility for real-world applications of more expensive and less plentiful materials. Indeed, the recycling of the spent sorbent for several sorption/desorption cycles offers significant benefits, including waste reduction and lower byproduct generation in dry FGD systems [17].

2.2. Sample Sources and Data from Suppliers

The hydrated lime sample (sample name: "PC") was synthesized and provided by Cimprogetti (Dalmine, BG, Italy) using a state-of-the-art planetary mixer capable of operating under controlled temperature and pressure conditions, suitable for producing dry hydrated limes with high specific surface areas. The supplier provided the following characteristics: BET Specific Surface Area = 35.9 m^2/g; BJH Desorption Pore Volume = 0.18672 cm^3/g; DH Desorption Pore Width = 14.57 nm. The high-silica 13X zeolite (sample name: "13X") was supplied by Honeywell UOP (Des Plaines, IL, USA). The supplier provided the following characteristics: SiO_2/Al_2O_3 = 1.27, Na_2O = 16.28 wt%, SSA_{BET} = 791 m^2g^{-1}, SSA_{microp} = 731 m^2g^{-1}, V_p = 0.301 cm^3g^{-1}, and V_{microp} = 0.267 cm^3g^{-1}.

2.3. Desulfurization Experiments

The experiments were conducted on a laboratory scale. Figure 1 depicts a schematic diagram of the experimental apparatus. The apparatus comprises a feed gas-flow control system, a fixed-bed reactor, a heating plate, a bubbler filled with deionized water for moist air, a micro-gas chromatograph (Micro GC Agilent 490 (Santa Clara, CA, USA)) for flue gas downstream analysis, and a tail gas treatment system. The temperature and humidity data acquisition (DaQ) system is described in the Supporting Information (SI1.2, see Figure S2).
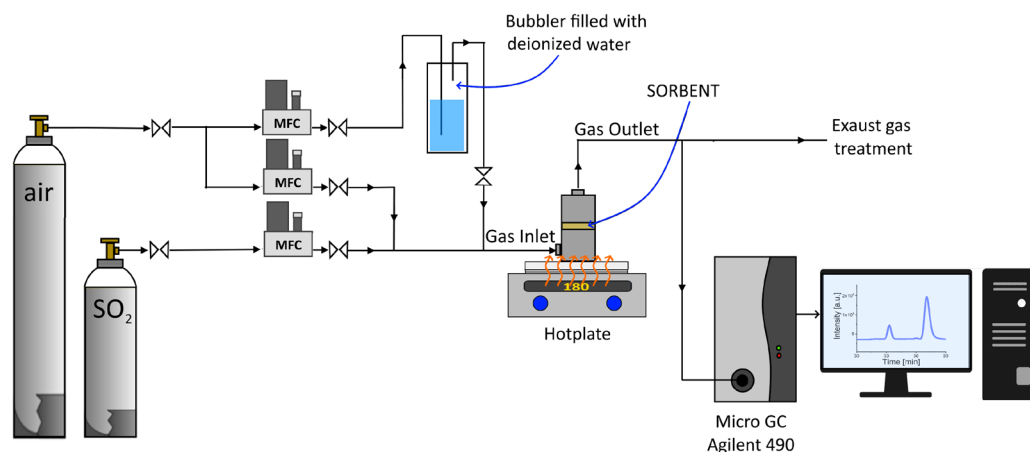

Figure 1. Schematic diagram of the experimental apparatus for the FGD experiments.

Figure S1a illustrates the main components of the reactor design. The cylindrical reactor has an outer height of 70 mm and a base diameter of 29 mm. The reactor consists of two blocks, their walls measuring 4 mm in thickness. The internal volume of the reactor is 21.46 cm^3. These geometrical specifications were used for the simulation described in Section 2.3.2. In order to prevent corrosion by sulfuric acid, which may be produced as a result of the chemical reactions indicated in (2) and (3) during the flow of vapors fed into the reactor during FGD experiments, the reactor body was constructed using AISI 316L steel (Figure S1b).

$$2SO_2(g) + O_2(g) \leftrightarrow 2SO_3(g) \tag{2}$$

$$SO_3(g) + H_2O(g) \leftrightarrow H_2SO_4(g) \tag{3}$$
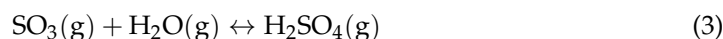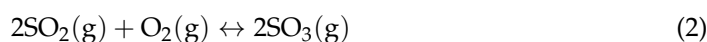
The reactor was designed to accommodate the adsorbents between two microfiber glass filters with a diameter of 25 mm (Whatman GF/A, Cleves, OH, USA), which were suspended at the connection point of the two blocks that comprise the reactor's body. To facilitate the loading and removal of the samples, a Teflon ring was placed between the two filters (Figure S1a,b). The ring has a thickness of 1.5 mm, with outer and inner diameters of 25 mm and 15 mm, respectively.

A heating plate (VELP Scientifica) was employed to increase the reactor temperature. The effective temperature in key geometric points of the reactor chamber was determined in situ using the experimental procedure described in the Supporting Information (SI1.2). In particular, thermocouple 5, located as shown in Figure S3, was utilized to ascertain the temperature within the sample holder containing the adsorbent. The effective temperatures of the samples during the FGD experiments were 75 or 160 °C, depending on the setting of the heating plate. The model calculation in Section 2.3.2. enabled the description of the temperature distribution along the reactor body. The reactor was connected to a flushing system via Swagelok connectors (7 mm in diameter), which carried the gas flow within Teflon tubes.

2.3.1. Gas Phase

Dry and wet synthetic air (20% O$_2$ and 80% N$_2$) and SO$_2$ (complement in air) from certified cylinders (N5.0 degree of purity) were fluxed through mass-flow controllers (Brooks

Instruments, Hatfield, PA, USA) and mixed before entering the fixed-bed reactor. Water vapor was added by bubbling a portion of the synthetic air stream into a bubbler containing deionized water (Figure 1). The relative humidity (RH%) within the reactor was monitored downstream using the DaQ system (Figure S2), in accordance with the Supporting Information. An extreme RH% will cause adsorbents to block and stick, preventing the scrubber from operating correctly in industrial applications. For this reason, the stream RH% content was set below 50% and evaluated in different RH% conditions, namely, at 30RH% and 45RH%. In all experiments, the total flow rate (comprising humid synthetic air and SO_2) was maintained at a constant value of 50 sccm.

2.3.2. Reactor Modeling

The model calculation was developed using the COMSOL Multiphysics® software v.6.2 [20] (National Research Council, CNR, campus license). The model is based on the reactor geometry and is presented in the Supporting Information (SI1.4). The geometry was reproduced using the Comsol drawing tool, as illustrated in Figure S4. The materials used in the model include 316L steel for the reactor body, "air" for the gas phase inside the reactor, and those injected as a flowing fluid. The porous sect is modeled as a disk made of slaked lime, $Ca(OH)_2$, with 30% porosity.

The physics involved in this model include the non-isothermal flow (laminar approximation) and heat transfer in solid and fluid media. The laminar flow (spf) interface is used to compute the velocity and pressure fields associated with the laminar flow of a single-phase fluid. A laminar flow persists as long as the Reynolds number is below a certain critical value. As the Reynolds number increases, the disturbances tend to grow, eventually leading to a transition to a turbulence regime. The equations solved by the laminar flow interface are the Navier–Stokes equations for conservation of momentum and the continuity equation for conservation of mass. The incorporation of a porous medium domain resulted in the addition of a Forchheimer Drag subnode to the physics interface. The simulation incorporates the effects of gravity, with the buoyancy force included in the Navier–Stokes equations. The Heat Transfer Module contains a number of features for modeling conjugate heat transfer and non-isothermal flow effects. Laminar flow is supported and can be modeled with natural and forced convection. Moreover, the simulation incorporates pressure work and viscous dissipation to model the temperature distribution. The Heat Transfer in Solids interface is used to simulate heat transfer in solids by conduction, convection, and radiation. The model is operational by default in all domains. All functionalities for including other domain types, such as a fluid domain, are used to differentiate the steel reactor, the porous disk, and the air domain within the reactor. The temperature equation defined in solid domains corresponds to the differential form of Fourier's law, which may contain additional contributions such as heat sources. As the system is heated from below by a heating plate, the bottom surface is maintained at a constant temperature (see Table S1) for the 180 and 370 °C cases, which are hereafter designated as the "A" and "B" cases, respectively. The only other boundary condition is the top surface of the reactor, which is set at the measured temperature values (see Table S1) for both cases. The model is exploited by combining two simulations: the first one is a steady-state model, which solely considers heat transfer to replicate the temperature distribution of the steel reactor. The second simulation is a transient model in which the fluid flow is activated, as well as the solid–fluid heat transfer and the non-isothermal fluid flow.

2.3.3. Analysis of Reaction Products

The concentration of SO_2 in the gas phase exiting the bed reactor was monitored at ≈4 min intervals using a Micro GC Agilent 490 with a thermal conductivity detector (TCD). The μGC was equipped with a Porous Layer Open Tubular (PoraPLOT U) column. According to the product details, this column is suitable for switching systems that analyze polar (e.g., SO_2) and apolar volatile compounds. Moreover, water elutes as a sharp and

quantifiable peak, making the retention times of target compounds repeatable, as they are not influenced by water in the sample. This last feature is crucial for the proposed FGD system since it enables the monitoring of SO_2 concentrations independently of stream humidity adjustment. The μGC measurement parameters are listed in Table S3. The carrier gas, column configuration (temperature and pressure), injector temperature and time, and sample time were chosen according to the 490 Micro Gas Chromatograph User Manual for the PoraPlot 10 m instrument. The backflush-time and run-time values were established following preliminary tests to provide a suitable chromatogram for evaluating SO_2 peak areas. Indeed, the representative chromatogram in Figure S5 shows very good peak separation between SO_2 and other gaseous components (H_2O and O_2). Figure S6 displays the linear calibration of SO_2 up to 1200 ppm with an R^2 of 0.99935. The data trends of the SO_2 concentration versus time were transmitted to an online computer and stored in a data file.

The actual SO_2 content in the stream flowing inside the reactor may be contingent upon the configuration of the reactor and the relative humidity content. Consequently, the concentration of SO_2 (in ppm) was evaluated over time for the two relative humidity conditions used in this study (30 and 45 RH%). The same configuration used for FDG measurements was maintained, i.e., a reactor loaded with two microfiber glass filters and a Teflon ring, devoid of adsorbent material. Figure S7 shows that, at equilibrium, the concentrations of SO_2 in the streams with 30 RH% and 45 RH% were 600 ppm and 580 ppm, respectively. Moreover, the experiments demonstrated a dead time of ≈5 min, during which minimal concentrations of SO_2 were detected from the μGC. To assess the effect of humidity on the SO_2 concentration and its reactor filling rate, Figure S7 also depicts the SO_2 concentration vs. time for dry conditions (4 RH%). This evidence demonstrates the absence of a dead time and the faster attainment of the equilibrium SO_2 concentration, namely, 610 ppm. The interaction of SO_2 with water vapor along the tubes or at the interface with the reactor walls and the sample holder may result in a slight delay in the attainment of equilibrium during FDG measurements. These experimental findings were integrated into the FDG data analysis, which included the determination of breakthrough curves, breakthrough times, and breakthrough sulfur capacities.

In each experiment, the breakthrough curve was measured until the dimensionless concentration (C/C_0) reached 0.90, where C_0 was the SO_2 air intake concentration obtained from Figure S7 and C was the outlet SO_2 concentration. Once this value is reached, the material removal efficiency becomes insufficient for effective utilization within the FGD process.

Figure S8 shows a schematic diagram of a breakthrough curve, which illustrates the parameters considered in this work for the comparison of different experimental conditions.

The breakthrough times (t_b) were determined with the objective of investigating the impact of temperature and relative humidity on the loss rate of adsorbent efficiency in the removal of the adsorbate. A longer breakthrough time indicates a reduced frequency of regeneration of the adsorbent, which is economically more viable [21]. In this study, the breakthrough time is defined as the time at which the instantaneous adsorbent removal efficiency reaches 90%. The instantaneous removal efficiency, η (%), represents the capacity of the adsorbent to remove the adsorbate at a specific point in time and is calculated as follows [15]:

$$\eta = \frac{(C_{blank} - C_{ads})}{C_{blank}} \times 100\% \tag{4}$$

where C_{blank} is the actual SO_2 intake concentration (mg/m^3) obtained from the measure of the blank after stabilization (see Figure S7) and C_{ads} is the outlet SO_2 concentration (mg/m^3) when the adsorbent is placed within the reactor.

After a period of latency, known as the lag phase, during which the fresh adsorbent contains a large number of available adsorption sites and thereby binds the adsorbate molecules consecutively, the removal efficiency usually starts to rapidly decrease [21,22], leading to the so-called logarithmic phase. The two phases of the breakthrough curve can

be described by the maximum specific breakthrough rate, μ_{max}, and the lag time, λ. As shown in Figure S8, μ_{max} represents the slope of the tangent line at the inflection point of the breakthrough curve, while λ denotes its t-axis intercept. In order to graphically obtain μ_{max}, the experimental points were fitted by a polynomial function.

The breakthrough sulfur capacity (mg/g), S, is defined as the total amount of SO_2 removed per gram of adsorbent in the breakthrough time, such that the concentration ratio (C/C_0) reaches 0.90 [15]. This is represented by the following equation:

$$S = \left[\sum_{ads=0}^{n} (C_{blank} - C_{ads}) \times t_0 \right] \times \frac{V}{G} \qquad (5)$$

where t_0 represents the data recording interval, V is the total flue gas flow (mL/min), and G is the quantity of desulfurizer (g).

Once the experiments had been completed, the sorbent was extracted from the reactor bed for further characterization measurements.

2.3.4. Theoretical Model

The dynamic adsorption behavior and the adsorption affinity of PC and 13X can be examined through different mathematical models. The Adams–Bohart, Yoon–Nelson, and Thomas models are mathematical models widely used to describe the dynamics of adsorption in a fixed-bed column. These models predict the breakthrough behavior of adsorbates in packed-bed systems and are based on simplifying assumptions. Each model's applicability depends on the specific experimental setup, desired accuracy, and available data. In summary, (i) the Adams–Bohart model is employed for preliminary design and estimation of bed height, (ii) the Yoon–Nelson model enables quick predictions of breakthrough time without needing detailed adsorption data, and (iii) the Thomas model provides capacity and kinetic evaluation under equilibrium conditions.

Based on our experimental setup, and given the expected fast reactivity of SO_2 with $Ca(OH)_2$, the equilibrium-driven assumption seemed the most reasonable; thus, from among the most widely used adsorption models, we chose the Thomas model to fit the entire breakthrough curve [23,24]. Indeed, the Thomas model had already been successfully applied to Ca-based adsorbents for SO_2 adsorption experiments in fixed-bed columns [25].

The satisfactory agreement of experimental data from the PC sample, here used as a standard material, and the theoretical model provide evidence that the experimental apparatus is suitable for FGD measurements.

Moreover, the Thomas model was used to calculate the Thomas rate constant, k_{TH} (mL min^{-1} mg^{-1}), and the predicted bed capacity at the equilibrium, q_0 (mg g^{-1}), from its linearized expression [24,26]:

$$ln\left(\frac{C_0}{C_t} - 1 \right) = \frac{k_{TH} q_0 m}{Q} - k_{TH} C_0 t \qquad (6)$$

where m is the mass of adsorbent in the reactor (g) and Q is the flow rate (mL min^{-1}). As the points at low C/C_0 prior to a dead time of 5 min described in Section 2.3.3 were due to the system configuration rather than the adsorbent uptake, those experimental points were removed from the calculation.

2.4. Material Characterization Techniques

The phase purity and crystallinity of the samples were examined by X-ray powder diffraction (XRPD). XRPD data were collected using the Bruker D8 Advance Da Vinci powder diffractometer, which operates in Bragg–Brentano geometry and is equipped with a Cu-anode X-ray tube, a Ni-filter to suppress Cu$K\beta$ component, and a LynxEye XE silicon strip detector set to discriminate Cu$K\alpha_{1,2}$ radiation. The sample was mounted on a PMMA (polymethyl methacrylate) holder with pseudo-lateral loading, and a knife, perpendicular to the sample, was placed at a suitable distance from the sample surface to reduce

the air-induced scattering. The samples were scanned in a continuous mode from 5 to 90° 2θ with a step size of 0.02° 2θ and a counting time of 2 s per step. Qualitative phase identification was conducted using the EVA software v.7.1 (Bruker), and the XRPD patterns obtained were refined using the Rietveld method (TOPAS v.7.0, Bruker and GSAS software in EXPGUI graphical interface), starting from the structural model reported by Guzzinati et al. (2018) for the same 13X used in this work [27].

The thermal behaviors of the samples were analyzed by thermogravimetric (TG) and differential thermal (DTA) analyses. TG analysis was carried out on both the unloaded and loaded powder samples under constant and controlled synthetic air-flow conditions using an STA 409 PC LUXX®—Netzch instrument (Gerätebau, Germany). The heating rate was set at 10 °C/min, with the temperature ranging from room conditions (RT) to 1200 °C. Approximately 30 mg of sample was used for each test. Alumina (Al_2O_3) was used as the control and standard.

Scanning electron microscopy (SEM) analyses were performed at the MEMA Center of the University of Florence (Italy). The samples were prepared by placing an aliquot of powder on double-sided conductive carbon tape on aluminum stubs. A carbon coating was applied to the top of the supports to ensure electrical conductivity. The choice of the carbon layer was made with the intention of providing preferential access to the microchemical information. Conversely, high-magnification morphological investigations (magnification: > 6000×) were affected by a certain amount of noise.

The samples were examined with a ZEISS EVO MA15 SEM equipped with an Oxford INCA 250 energy-dispersive X-ray (EDS) spectrometer for microanalysis. The operating accelerating voltage was maintained at 20 kV. The EDS peak quantification was automatically performed by Gaussian fitting of the peak profile, considering corrections for atomic number, absorption, and fluorescence (ZAF). Although the EDS microchemical information was semi-quantitative in nature, the spectral response was calibrated with respect to a metallic Co reference sample analyzed under the same conditions.

All samples were subjected to at least 6 different microanalyses: 3 different raster analyses were conducted at 500× magnification over the whole analytical field, while 3 different point analyses were performed at three points of a further analytical field at a magnification of 4000×. For all fields, high-resolution morphological micrographs were obtained using either secondary electrons (SEs) or backscattered electrons (BSEs) or both.

X-ray photoelectron spectroscopy (XPS) measurements were conducted using a Kratos AXIS Ultra^DLD instrument (Kratos Analytical, Manchester, UK) equipped with a hemispherical analyzer and a monochromatic Al K*α* X-ray source (1486.6 eV) in spectroscopy mode. For the measurements, the powders were deposited on carbon tape and placed on a silicon support. Samples were analyzed at a 0° take-off angle between the sample surface normal and the analyzer axis, corresponding to a sampling depth of approximately 10 nm. A survey spectrum (binding energy range: −5 to 1350 eV) was acquired for each sample to identify surface elements. High-resolution spectra of the Ca 2p, O 1s, C 1s, and S 2p core levels were subsequently collected. XPS quantification was performed using instrument sensitivity factors and high-resolution spectra. Alignment was achieved by setting the C 1s peak, related to hydrocarbons, at 285 eV. All XPS data were analyzed using previously described software [28].

3. Results and Discussion

3.1. Modeling

The internal temperature distribution of the reactor and the porous disk, as well as the velocity field of the air flow, were obtained through the use of COMSOL Multiphysics® software [20], as described in Section 2.3.2. The internal temperature distributions depicted in Figure 2a,b were compared with the measured values (Table S1) to validate the model. The discrepancy between the computed and measured values was 77 °C vs. 75 °C (case A) and 150 °C vs. 158 °C (case B).
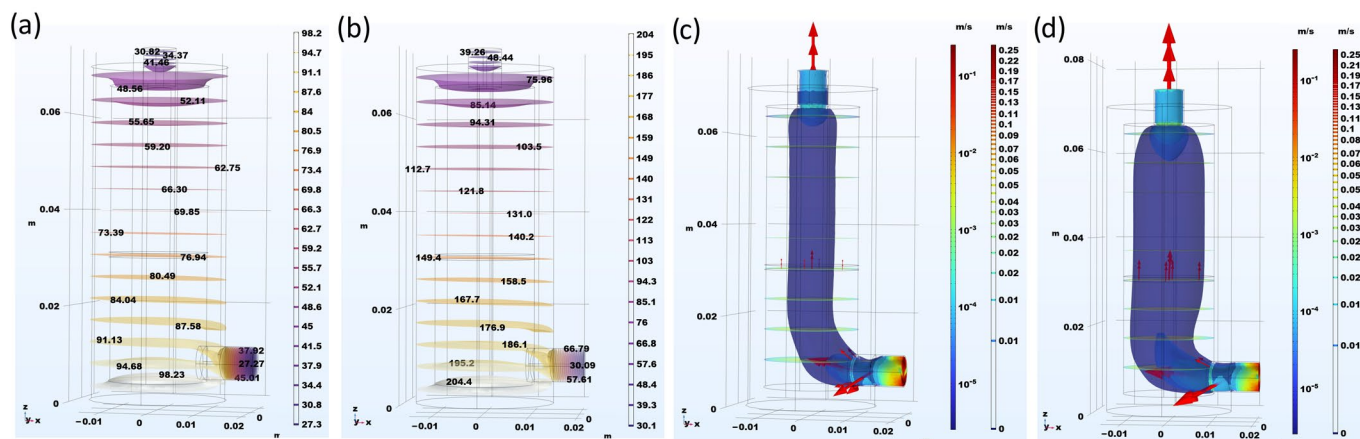
Figure 2. Temperature within the reactor computed for (**a**) case A (heater temperature of 180 °C) and (**b**) case B (heater temperature of 370 °C). The scale legends to the right of the models in (**a**,**b**) connect the temperature data with a color gradient. The computed velocity fields for cases A and B are shown in (**c**,**d**). The scale legends on the right of the models in (**c**,**d**) connect the flow velocity values with a color gradient. The red arrows indicate the direction of the flux.

The computed velocity field was concentrated in the center of the reactor and the porous disk in both cases, as shown in Figure 2c,d. The velocity fields for 180 and 370 °C exhibited only minor differences. This was due to the fact that the temperature of the air itself remained relatively constant, with outlet temperatures of 28 °C for A and 34 °C for B. Consequently, the inner system can be described as a flow of air that has a temperature of 25.5 °C at the bottom of the reactor, which gradually increases until it interacts with the porous media at 77 and 150 °C (for cases A and B, respectively). This means that the reaction between the SO_2 carried by the air flow and the adsorbent substrate likely occurs at the temperature of the porous media.

3.2. System Validation with Slaked Lime

3.2.1. Fixed-Bed FGD Experiments

Figure 3 shows the breakthrough curves for PC obtained under different experimental conditions, conducted for the purpose of validating the dry fixed-bed FGD system. The samples are labeled according to FGD temperature and RH%, as indicated in Table 1. The discussion that follows will also include the parameters λ and μ_{max} (see Figure S8) and the breakthrough sulfur capacity (mg/g) (obtained from Equation (5)), presented in Table 2.

Figure 3a displays the effect of varying the quantity of the sample within the reactor on the desulfurization process conducted at 75 °C and 30RH%. An increase in weight of the adsorbent from 0.10 g to 0.14 g resulted in a rise in both the t_b and λ parameters. On the other hand, the maximum specific breakthrough rate (μ_{max}) exhibited similar values in both breakthrough curves, indicating that the adsorbent quantity had a minimal impact on this parameter. The breakthrough sulfur capacity in both experiments was 18 mg/g, as this value was normalized by the PC weight. Notably, the breakthrough lag phase was very short when 0.10 g of PC was utilized. This may be attributed to the low ratio of adsorbent employed to inlet SO_2 adsorbate concentration [17]. Additionally, the geometry of the sample holder within the reactor may have influenced the shape of the breakthrough curve. Indeed, the vertical path of the flux along the adsorbent in the configuration described in Section 2.3 is relatively thin (1.5 mm) compared to that of other tubular reactors described in the literature [29]. Therefore, 0.10 g of adsorbent is considered the sample weight limit for loading the reactor to study the uptake capabilities of the material under these conditions. The desulfurization experiment with 0.14 g of PC at 75 °C in a humidified stream at 30RH% was replicated three times to evaluate the repeatability of the fixed-bed FGD experiments. Data plotted in Figure 3b highlight that the breakthrough curves look very similar. The breakthrough sulfur capacities are 18, 19, and 20 mg/g, indicating

that the results are reproducible, with an error of 1 mg/g. An increase in the reactor temperature resulted in a notable variation in all breakthrough variables (Figure 3c). Indeed, at 160 °C, the breakthrough sulfur capacity was 24 mg/g. Conversely, an increase in stream humidity at 45RH% resulted in a slight increase in the breakthrough sulfur capacity of PC [75 °C_45RH%] to 21 mg/g (Figure 3d). Both humidity and temperature exert an influence on the sulfur uptake process, resulting in prolonged t_b and λ. In addition, the breakthrough curve of PC [160 °C_30RH%] is distinguished by a more rapid increase in C/C_0 during the logarithmic phase and a longer time to reach the stationary phase. This refers to the condition in which the adsorbent approaches saturation [22].
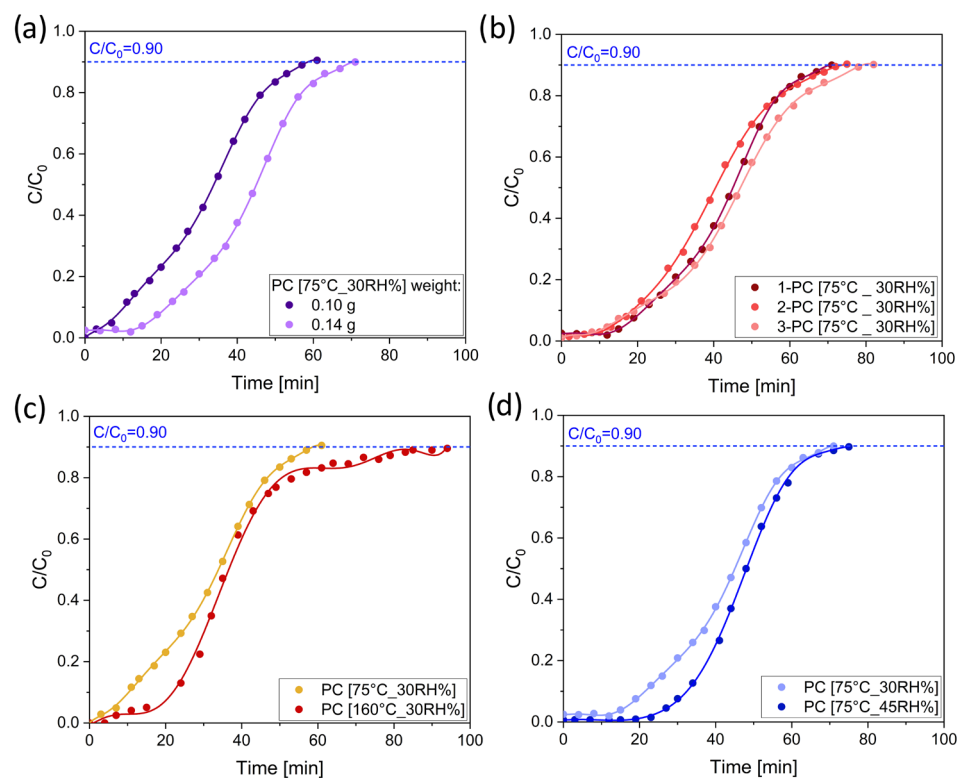
Figure 3. (**a**) Breakthrough curves obtained from different PC quantities, namely, 0.10 g and 0.14 g. C_0 = 600 ppm SO_2, uptake temperature = 75 °C, and 30RH%. (**b**) Breakthrough curves of PC collected in triplicate for repeatability evaluation. C_0 = 600 ppm SO_2, adsorbent quantity = 0.14 g, uptake temperature = 75 °C, and 30RH%. (**c**) Breakthrough curves for PC samples at 75 °C and 160 °C. C_0 = 600 ppm SO_2, adsorbent quantity = 0.10 g, and 30RH%. (**d**) Breakthrough curves for PC samples at 30 RH% and 45 RH%. C_0 = 600 ppm and 580 ppm SO_2, respectively; adsorbent quantity = 0.14 g; uptake temperature = 75 °C.

Table 1. Experimental conditions and labels for portlandite. The values in the "Temperature" column refer to the temperature of the adsorbent during the FGD experiments, which correspond to position 5 in Table S1.

Adsorbent Material	Temperature	RH%	SO$_2$ Concentration	Label
Portlandite	75 °C	30%	600 ppm	PC [75 °C_30RH%]
Portlandite	75 °C	45%	580 ppm	PC [75 °C_45RH%]
Portlandite	160 °C	30%	600 ppm	PC [160 °C_30RH%]
Portlandite	75 °C	30%	600 ppm	PC [75 °C_30RH%]

Table 2. Breakthrough sulfur capacity (mg/g) of PC in different conditions of temperature and RH%.

Sample	Weight	λ	t_b	μ_{max}	Breakthrough Sulfur Capacity
PC	0.10 g	16 min	10 min	0.027	18 mg/g
1-PC [75 °C_30RH%]					19 mg/g
2-PC [75 °C_30RH%]	0.14 g	28 min	20 min	0.029	18 mg/g
3-PC [75 °C_30RH%]					20 mg/g
PC [160°C_30RH%]	0.10 g	21 min	20 min	0.034	24 mg/g
PC [75°C_45RH%]	0.14 g	33 min	30 min	0.033	21 mg/g

The increase in breakthrough sulfur capacity at 45RH% compared to 30RH% can be attributed to the formation of liquid-film water molecular layers with extended thicknesses at higher moisture levels. Indeed, such films of water molecules promote SO_2 dissolution, enhancing the reaction kinetics at the adsorbent surface. The wetter the surface of the adsorbent, the more SO_2 might be dissolved from the flue gas, accelerating the process of desulfurization. The effect of different relative humidities on the desulfurization efficiency of Ca-based adsorbents has been widely discussed in previous studies [30,31].

The more pronounced performance shift caused by increasing the reactor temperature, on the other hand, was explored in greater depth in the current study via $Ca(OH)_2$ characterizations (see Section 3.2.3).

The breakthrough sulfur capacity values agree well with those previously reported in the literature, where Ca-based materials were used as adsorbents in dry fixed-bed FGD experiments (see Table S4; [15,32–39]). The obtained experimental results (Table 2) validate the experimental apparatus for mild desulfurization tests.

3.2.2. Application of the Thomas Model

Figure S9 shows the results of the linearized Thomas model, as described by Equation(6), as a linear plot of $\ln(C_0/C_t-1)$ against time, at various operational conditions. The Thomas parameters, calculated with linear fitting, are summarized in Table S5.

The Thomas model assumptions, namely, pseudo-second-order adsorption kinetics and negligible external resistance during the mass transfer processes, appear to be satisfied for 0.10 and 0.14 g of PC [75 °C_30RH%] and 0.14 g of PC [75 °C_45RH%], as evidenced by their correlation coefficient values ($R^2 > 0.95$). In these FGD experiments, the results for the adsorption capacity parameter, q_0, were found to be consistent with the values calculated by numerical integration of the experimental data. Indeed, the calculated q_0 is slightly higher than the corresponding breakthrough sulfur capacity in Table 1, which was calculated using the experimental point until $C/C_0 = 0.9$. In contrast, the fitting of the data for PC [160 °C_30RH%] yielded a relatively low R^2 value of 0.83, indicating that the Thomas model may not be as effective in this case.

The satisfactory agreement between the experimental data and the theoretical Thomas model for the PC adsorbent at 75 °C provides further evidence that the experimental apparatus is suitable for FGD measurements. The following paragraph provides an interpretation of the deviation of the PC [160 °C_30RH%] experiment from the model-based PC characterization before and after the FGD process.

3.2.3. PC Characterization

The results of the FGD experiments for the PC sample indicated that the increase in temperature was more sensitive than the relative humidity in terms of the uptake observed. Consequently, the characterization of PC was based on experimental findings to explain the differences between the reactions of PC with SO_2 at 75 °C and 160 °C.

The XRPD patterns of the pristine PC, PC [75 °C_30RH%], and PC [160 °C_30RH%] are presented in Figure S10. The unit-cell and structural parameters were determined starting from the trigonal *R*-3*c* (for calcite) and the trigonal *P*-3*m*1 (for portlandite) space groups. The PC samples exhibited the characteristic peaks of crystalline portlandite

(~96 wt%) and calcite (~3 wt%), as reported in Table S6. No evidence of a loss of crystallinity or the formation of new secondary phases was observed after the SO_2 uptake experiments. In PC samples, the SO_2 uptake was not clearly identified by diffraction data and unit-cell variations (Table S7).

Figure S11 illustrates that the PC samples exhibited a multistep weight loss in three distinct temperature ranges, with a total weight loss from 27 wt%, for the samples subjected to a gas flux at different temperatures, to 31 wt%, for the unloaded sample (Figure S11a). The first temperature range, up to approximately 400 °C, is marked by an endothermic event with a peak centered at approximately 100 °C (Figure S11c). This phenomenon is commonly associated with a dehydration reaction, which is the result of the release of surface-bonded water molecules. The transitions between the three thermal ranges, beginning at about 400 and 675 °C, are characterized by an endothermic and an exothermic reaction with peaks centered at approximately 500 and 750 °C. These reactions typically occur in samples of portlandite and calcite, where the release of hydroxyl and CO_2 molecules occurs during the decomposition processes of these phases in the temperature ranges of 390–485 °C and 600–870 °C, respectively [40,41].

In order to experimentally prove SO_2 chemisorption over the adsorbent surface, further experimental techniques were required for the PC samples. Therefore, EDS and XPS analyses were also performed.

The results of the micromorphological investigation indicate that the process of SO_2 adsorption carried out within the reactor did not significantly alter the size of the particles or their state of aggregation. This observation can be clearly discerned by comparing the micrographs of the pristine portlandite (PC) (Figure S12a) with those of [PC_75 °C_30RH%] and [PC_160 °C_30RH%] (Figure S12b,c). With regard to the microchemical investigation, the SEM-EDS measurements performed on PC samples corroborate their composition with respect to the major and minor components, namely, Ca, Mg, and O (Table S8). Carbon was detected, but its content was not quantified due to the carbon coating procedure used for the sample preparation. In addition to the aforementioned elements, Al, Si, P, and Sr were occasionally identified, just above their respective detection limits. The slight oxygen deficiency observed in all analyses can be ascribed to the well-known difficulty of accurately dosing light (Z < 9) elements using EDS. The most striking feature of the microchemical results presented in Table S8 is the S content, which appears below the detection limit in PC but is unquestionably present in PC [75 °C_30RH%] and PC [160 °C_30RH%], with values exceeding 1.0 wt%. The S content in PC [160 °C_30RH%], which exhibited the highest breakthrough sulfur capacity, is slightly greater than that observed in PC [75 °C_30RH%]. This suggests that elevated temperatures promote the formation of stable sulfur-based species, potentially due to uptake of SO_2. Indeed, as the FGD temperature increases, the Gibbs free energy of the system decreases, while significant molecular movement accelerates the chemical process [15].

To further investigate the presence of SO_2-derived species on the surface of PC, XPS analysis was conducted. The elemental analysis revealed the exclusive presence of Ca, O, C, and S in the samples. Quantitative analysis, presented in Table S9, indicated that S was absent in pristine PC, while PC [75 °C_30RH%] and PC [160 °C_30RH%] exhibited comparable concentrations of S-based species on their surfaces.

To ascertain the chemical nature of the species absorbed on the PC surface, high-resolution spectra of S 2p were collected (Figure 4). PC [75 °C_30RH%] displayed a doublet at 167.0 and 168.2 eV, which corresponded to S $2p_{3/2}$ and S $2p_{1/2}$ of $CaSO_3$, respectively [42,43]. In contrast, PC [160 °C_30RH%] showed an additional S 2p doublet, corresponding to $CaSO_4$ (S $2p_{3/2}$ at 169.0 eV and S $2p_{1/2}$ at 170.2 eV), alongside the S 2p doublet related to $CaSO_3$ [13,42,43].
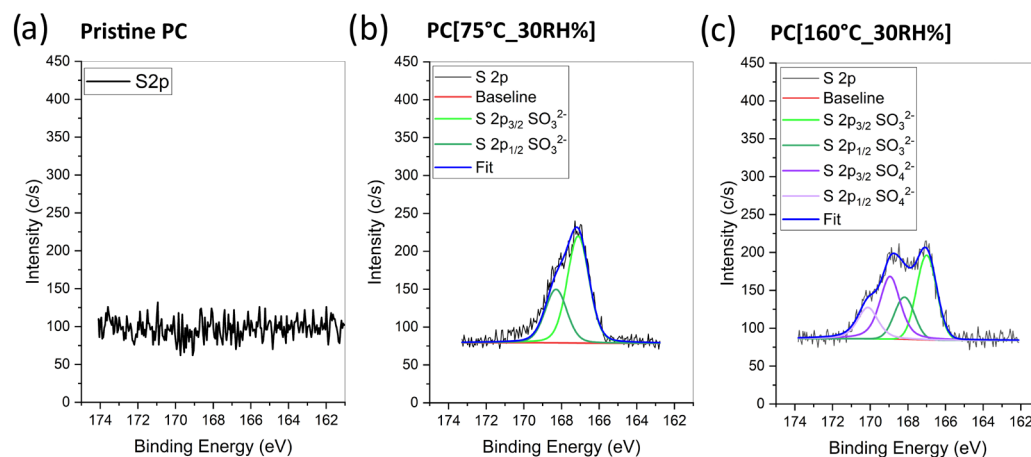
Figure 4. High-resolution spectra of S 2p core levels for: (**a**) pristine PC; (**b**) PC exposed to SO_2 at 75 °C and 30 RH%; (**c**) PC exposed to SO_2 at 160 °C and 30 RH%.

The ratio of S in $CaSO_4$ to S in $CaSO_3$ was approximately 50:50 (Table S10). These findings indicate that, at low temperatures, SO_2 tends to adsorb on the surface of PC as $CaSO_3$, following reaction (7). Conversely, an increase in temperature during the uptake of SO_2 results in the formation of both $CaSO_3$ and $CaSO_4$ species. This is likely due to the oxidation of adsorbed SO_3 at high temperatures [42,43], as in reaction (8).

$$Ca(OH)_2(s) + SO_2(g) \rightarrow CaSO_3(s) + H_2O(g) \tag{7}$$

$$CaSO_3(s) + \frac{1}{2}O_2(g) \rightarrow CaSO_4(s) \tag{8}$$
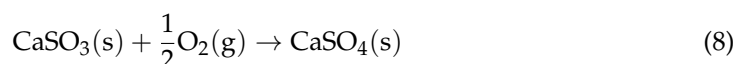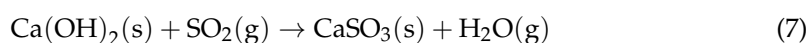
Therefore, the Thomas model's assumption of a Langmuir kinetic, described by a pseudo-second-order reaction, could be validated only for PC [75 °C_30RH%]. For PC [160 °C_30RH%], both reactions (7) and (8) contributed to the system uptake kinetics, deviating from simple modeling.

3.3. FGD Through Zeolite 13X

3.3.1. Fixed-Bed FGD Experiments

In order to investigate the impact of different properties of adsorbent materials on FGD in mild settings, namely, at low reactor temperatures (T < 100 °C) and low SO_2 concentrations, the SO_2 uptake capacity of $Ca(OH)_2$ was compared with that achieved through the deployment of zeolite 13X under analogous operational conditions. Specifically, FGD experiments were conducted at 75 °C, relative humidities of 30RH% and 45RH%, and 600 ppm of SO_2. The samples were labeled based on FGD temperature and RH%, as indicated in Table 3. The discussion that follows will also include the parameters λ and μmax and the breakthrough sulfur capacity (mg/g) presented in Table 4.

Table 3. Experimental conditions and labels for zeolite 13X. The values in the "Temperature" column refer to the temperatures of the adsorbent during the FGD experiments, which correspond to position 5 in Table S1.

Adsorbent Material	Temperature	RH%	SO_2 Concentration	Label
13X Zeolite	75 °C	30%	600 ppm	13X [75 °C_30RH%]
13X Zeolite	75 °C	45%	580 ppm	13X [75 °C_45RH%]

The breakthrough curves of 13X in Figure 5 are markedly different from those of PC in Figure 3, indicating that 13X exhibits an enhanced SO_2 uptake capacity. Such an improved FGD performance can be attributed to the greater surface area available for SO_2

adsorption of the zeolite in comparison to PC (i.e., 791 m^{2}g^{-1} vs. 35.9 m^{2}g^{-1}, respectively). Moreover, the zeolite surface sites exhibited notable catalytic activity, which may have boosted the adsorbent properties of this material. As the RH% increased, both the t_b and λ values increased, yet the breakthrough sulfur capacity was significantly reduced. It can be observed that the μ_{max} value of 13X [75 °C_30RH%] is approximately half that of 13X [75 °C_45RH%], indicating a slower decay in removal efficiency over time. This results in SO$_2$ uptakes of 51 mg/g for 13X [75 °C_30RH%] and 41 mg/g for 13X [75 °C_45RH%] (see Table 4). 13X characterizations before and after the FGD experiments were used to explain the influence of humidity on the breakthrough curve results.

Table 4. Breakthrough sulfur capacity (mg/g) of 13X in different conditions of RH%.

Sample	Weight	λ	t_b	μ_{max}	Breakthrough Sulfur Capacity
13X [75 °C_30RH%]	0.14 g	27 min	30 min	0.0076	51 mg/g
13X [75 °C_45RH%]	0.14 g	42 min	45 min	0.015	41 mg/g
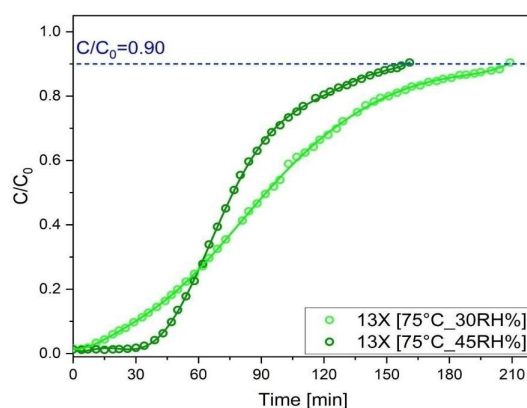
Figure 5. Breakthrough curves for 13X adsorbents at 30 RH% and 45 RH% and C$_0$ = 600 ppm and 580 ppm SO$_2$, respectively; adsorbent quantity = 0.14 g; uptake temperature = 75 °C.

The uptake capacities of zeolite 13X are compared to those of other zeolites in Table S4.

3.3.2. Application of the Thomas Model

Figure S13 shows the results of the linearized Thomas model (Equation (6)) as a linear plot of ln(C$_0$/C$_t$−1) against time under varying operational conditions. The Thomas parameters, obtained from the linear regression, are summarized in Table S11.

The R^2 values obtained for 13X [75 °C_30RH%] and 13X [75 °C_45RH%] were 0.95 and 0.92, respectively, indicating a best fit to the experimental data at lower humidity conditions. Figure S13 shows a clear deviation from linearity for 13X [75 °C_45RH%] between 5 and 30 min. This is attributed to the low values of C/C$_0$ observed in the breakthrough curve (Figure 5).

The k_{TH} value was approximately twice as high for 13X [75 °C_45RH%] as for 13X [75 °C_30RH%], in accordance with the μ_{max} values reported in Table 2. Furthermore, the results for the adsorption capacity parameter, q_0, were found to be in accordance with the values calculated by the numerical integration of the experimental data.

3.3.3. 13X Characterization

The XRPD patterns of pristine 13X, 13X [75 °C_45RH%], and 13X [75 °C_30RH%], presented in Figure S14, evidence the high crystallinity of these samples, which exhibit characteristic peaks of zeolite with an FAU topology and a minimal contribution of LTA-type zeolite. At low 2Θ angles, both the position and intensity of the X-ray diffraction peaks exhibited differences between the unloaded and loaded 13X samples, suggesting that the zeolite structure is affected by exposure to SO$_2$. According to the literature, the zeolite

adsorptive desulfurization of SO_2 encompasses both physisorption and chemisorption processes [44]. In contrast to PC, 13X is characterized by the presence of primary porosities (referred to as supercages or α-cages) accessible through a 12-ring window (12R) with a diameter $\approx$6 Å interconnected by windows with a diameter of $\approx$7.4 Å.

The chemisorption of SO_2 in these large windows and supercages can occur by sulfur-sorbent π-complexation and sulfur–metal (S-M) direct coordinate bonding. On the other hand, the filling of the zeolite microporous adsorption space, as with slaked lime, can be considered a physisorption process. Moreover, the adsorbed molecule diffuses within a zeolite channel and becomes subjected to diverse energy fields, which are characterized by different potentials (i.e., polaritazion) [45]. This encompasses both monolayer and multilayer adsorption, as well as capillary condensation [13]. Our results indicate that the structure of the zeolite samples was affected by exposure to SO_2. After the FGD experiments, the decrease in the crystallite size (Table S12) in both 13X [75 °C_45RH%] and 13X [75 °C_30RH%] was concomitant with variations in the unit-cell volume (Table S13) as well as bond distances and angles in comparison to the pristine sample (Table S14).

Tables S14 and S15 show the structural details and the atomic bond distances O1–O1 and O4–O4 limiting the 12-ring windows. All these features indicated the phenomenon known as "adsorption-induced deformation" due to the interactions between the adsorbate and the zeolite pore walls [46,47]. The deformation pattern can be affected by several factors, such as limitations of the pore size and pore shape, the surface chemistry of the adsorbent, as well as interactions of the adsorbate molecules with the extra-framework cations and framework oxygens of the zeolite. The extra-framework content in zeolites is related to the zeolite framework type and the Si/Al ratio, and it affects the enthalpy of adsorption of gases in these materials [18]. According to Emelianova et al. [46] and Nasluzov et al. [48], SO_2 and the 13X framework can interact by donor–acceptor interactions and hydrogen bonding.

An alternative bridging mechanism proposes that both oxygens of the captured gas interact with distinct extra-framework cations of the zeolite. However, it is more accurate to refer to the entrance of the gas into the zeolite cavities rather than the surface contact when discussing the steady growth of parameters, such as the total unit-cell volume and the crystallographic free area (CFA) (Table S12 and Table S15, respectively). The latter is derived from the combination of the O1–O1 and O4–O4 bond distances of the oxygen framework [15]. Specific features, such as a framework topology and the type/location of the charge-balancing cations, can affect the deformation mechanism; thus, when the pore is loosely filled with the adsorbate, the adsorbing molecules can exert a pressure on the pore walls, thus deforming the zeolite framework, as was observed for 13X. Notably, the increase in the unit-cell volume as well as the pore apertures (CFAs) (Table S12 and Table S15, respectively) were more pronounced in 13X [75 °C_45RH%] than in 13X [75 °C_30RH%]. The diffusion of both H_2O and SO_2 through the zeolite framework can potentially be attributed to two concomitant factors: increased hydration of 13X at 45RH% or higher sulfur uptake during the FGD process. To gain further insight into the two systems, thermogravimetric (TG) and microchemical EDS analyses were performed.

Figure S15 shows the thermal behavior of the 13X zeolite samples. The pristine zeolite displayed the most significant weight loss during the heating process in comparison to the zeolites in the uptake experiments. The 13X samples showed a weight loss of $\approx$25 wt% for the pristine sample and 20 wt% after the FGD experiments. The weight loss at low temperatures (up ~150 °C) indicates both SO_2 and water molecules physiosorbed on the surface. This process is accompanied by endothermic reactions, as evidenced by the DTA data. A further weight loss took place and persisted until approximately 400 °C. This phenomenon can be ascribed to the chemosorbed water molecules, which were trapped as extra-framework species in all the samples. The exothermic peak at ~850 °C is associated with structural zeolite collapse. Slight differences in the maxima at high temperatures are indicative of differences in thermal stability. This last may be attributed to the presence

of guest molecules within the zeolite structure which could have modified the thermal behavior of the material [49].

Micromorphological investigation revealed that the FGD experiments did not significantly alter the size of 13X particles or their state of aggregation (see Figure S16). The SEM-EDS measurements performed on zeolite samples corroborate their composition with respect to the major and minor components, namely, Na, Al, Si, and O (see Table S16). In addition to the aforementioned elements, Ca and Cl were occasionally observed in the zeolite samples, just above their respective detection limits. The slight oxygen deficiency observed in all analyses can be ascribed to the well-known difficulty of the EDS system in accurately dosing light (Z < 9) elements.

It is noteworthy that while the breakthrough sulfur capacity of 13X [75 °C_30RH%] was significantly higher than that of 13X [75 °C_45RH%], the S contents of both samples after the uptake measurement were nearly identical, namely, 3.69 and 3.82 wt%, respectively. This phenomenon may be attributed to a reduction in the stability of the SO_2 adsorbate generated at a lower RH%, which would have been desorbed from 13X [75 °C_30RH%] shortly after the FGD process. Indeed, the presence of water molecules may exert two opposing effects on the uptake process. On the one hand, both H_2O and SO_2 may compete for the same adsorption sites [50]. This would result in a reduction in the breakthrough sulfur capacity of 13X, as observed when the humidity was increased from 30RH% to 45RH%. Conversely, intrazeolitic water may facilitate the sorption of SO_2 through the zeolite framework by the Grotthuss mechanism, which works as a carrier [51]. This possibility entails the formation of H_2SO_3 within the Na-Y zeolite cavities [51,52]. The enhanced stability of the trapping of the SO_2 derivatives adsorbed within the microporosities of the zeolite may explain why 13X [75 °C_45RH%] appears to retain a greater quantity of S-based compounds than 13X [75 °C_30RH%].

4. Conclusions

This study successfully developed and validated a laboratory-scale pilot system based on a dry fixed-bed reactor for FGD experiments under mild conditions (75/160 °C and 30/45 RH%). The system was systematically monitored using a custom-designed data acquisition system and mass-flow controllers. COMSOL Multiphysics software provided valuable insights into the reactor's internal temperature distribution and air-flow operational dynamics.

Two materials, portlandite and 13X zeolite, were used to validate the system. The breakthrough sulfur capacity of PC was consistent with the existing literature. Furthermore, the breakthrough curves indicated that an increase in temperature had a more pronounced favorable effect on PC absorption than an increase in relative humidity. It can be reasonably assumed that at a temperature of 160 °C, the PC catalytic activity in relation to SO_2 chemisorption will increase. 13X zeolite exhibited a superior breakthrough sulfur capacity to PC, due to its microporosity, large surface area, and high catalytic activity. XRPD analyses revealed that 13X underwent structural changes upon interaction with H_2O and SO_2, highlighting its potential for efficient sulfur capture. Notably, the breakthrough sulfur capacity of 13X zeolite was higher at 30%RH, suggesting the complex role of water in facilitating or hindering sulfur adsorption.

The results underscore the potential of dry fixed-bed FGD systems, particularly in applications where sulfur capture from flue gases is critical, as in the petrochemical industry. These systems offer significant advantages, including high efficiency, scalability, and operational flexibility under varying environmental conditions. Future research should focus on optimizing material properties, system design, and operating conditions to further enhance sulfur capture efficiency and develop robust solutions for large-scale industrial applications, including the petrochemical sector. Continued exploration of the interaction between temperature, humidity, and adsorbent materials will be essential to fine-tune performance and ensure sustainable, cost-effective sulfur removal.

Author Contributions: M.M. (Maura Mancinelli) and E.S. contributed equally to this work. M.M. (Maura Mancinelli) contributed to the conceptualization, methodology, validation, writing (original draft), investigation and material characterization, and data curation and supervision. E.S. contributed to the conceptualization, methodology, validation, writing (original draft), FGD experiments, and data curation and supervision. F.D.B. contributed to the methodology, investigation and material characterization, and writing (review and editing). V.C. contributed to the methodology and writing (review and editing). M.V. contributed to the methodology and writing (review and editing). G.M. contributed to the data curation and supervision and writing (original draft). L.B. contributed to the methodology and data acquisition. L.V. contributed to the investigation and material characterization. A.G. contributed to the investigation and material characterization and writing (review and editing). G.V. contributed to the investigation and material characterization and writing (review and editing). M.M. (Mattia Massa) contributed to the writing (review and editing). A.M. contributed to

References

1. Laurent, A.; Espinosa, N. Environmental Impacts of Electricity Generation at Global, Regional and National Scales in 1980–2011: What Can We Learn for Future Energy Planning? *Energy Environ. Sci.* **2015**, *8*, 689–701. [CrossRef]
2. Fioletov, V.E.; McLinden, C.A.; Krotkov, N.; Li, C.; Joiner, J.; Theys, N.; Carn, S.; Moran, M.D. A Global Catalogue of Large SO_2 Sources and Emissions Derived from the Ozone Monitoring Instrument. *Atmos. Chem. Phys.* **2016**, *16*, 11497–11519. [CrossRef]
3. Srivastava, R.K.; Jozewicz, W. Flue Gas Desulfurization: The State of the Art. *J. Air Waste Manag. Assoc.* **2001**, *51*, 1676–1688. [CrossRef]
4. Rossi, A.; Spagnoli, E.; Visonà, A.; Ahmed, D.; Marzocchi, M.; Guidi, V.; Fabbri, B. SO_2 Detection over a Wide Range of Concentrations: An Exploration on MOX-Based Gas Sensors. *Chemosensors* **2024**, *12*, 111. [CrossRef]
5. Flagiello, D.; Erto, A.; Lancia, A.; Di Natale, F. Simultaneous Absorption of SO_2 and NO_x from Simulated Flue-Gas Exploiting the Enhancing Oxidative Ability of Aqueous Euchlorine as Scrubbing Solution. *Fuel* **2024**, *368*, 131611. [CrossRef]
6. Brandt, P.; Nuhnen, A.; Lange, M.; Möllmer, J.; Weingart, O.; Janiak, C. Metal–Organic Frameworks with Potential Application for SO_2 Separation and Flue Gas Desulfurization. *ACS Appl. Mater. Interfaces* **2019**, *11*, 17350–17358. [CrossRef]
7. Ng, K.H.; Lai, S.Y.; Jamaludin, N.F.M.; Mohamed, A.R. A Review on Dry-Based and Wet-Based Catalytic Sulphur Dioxide (SO_2) Reduction Technologies. *J. Hazard. Mater.* **2022**, *423*, 127061. [CrossRef]
8. Li, X.; Han, J.; Liu, Y.; Dou, Z.; Zhang, T. Summary of Research Progress on Industrial Flue Gas Desulfurization Technology. *Sep. Purif. Technol.* **2022**, *281*, 119849. [CrossRef]
9. Marketgrowthreports. Global Flue Gas Desulfurization (FGD) Market Research Report 2024. Available online: https://www.marketgrowthreports.com/global-flue-gas-desulfurization-fgd-market-26635041 (accessed on 15 September 2024).
10. Inkwoodresearch. Global Flue Gas Desulfurization Market Forecast 2023–2032. Available online: https://inkwoodresearch.com/reports/flue-gas-desulfurization-market/ (accessed on 15 September 2024).
11. Wu, C.; Sun, Z.; Ye, C.; Qi, Z.; Chen, J.; Huang, Z.; Qiu, T. Encapsulation of HPW and Preparation of Composites Rich in Zr-Defects by Manual Grinding: Synergistic Catalysis for Efficient Oxidative Desulfurization at Room Temperature. *Chem. Eng. J.* **2023**, *451*, 138906. [CrossRef]
12. Wang, A.; Li, S.; Zheng, Q.; Zhang, S.; Zhang, S.; Wang, Z.; Liu, Z.; Yan, K. Study on the Effects of Wet Flue Gas Desulfurization on Particulate Matter Emission from Industrial Coal-Fired Power Plants. *Separations* **2023**, *10*, 356. [CrossRef]
13. Chang, J.; Liu, M.; Wan, J.; Shi, G.; Li, T. Preparation of High-Reactivity Ca-Based SO_2 Adsorbent and Experimental Study for Simulated Flue Gas Dry Desulfurization. *Energy Rep.* **2023**, *9*, 85–95. [CrossRef]
14. Mathieu, Y.; Tzanis, L.; Soulard, M.; Patarin, J.; Vierling, M.; Molière, M. Adsorption of SO_x by Oxide Materials: A Review. *Fuel Process. Technol.* **2013**, *114*, 81–100. [CrossRef]
15. Xing, G.; Wang, W.; Zhao, S.; Qi, L. Application of Ca-Based Adsorbents in Fixed-Bed Dry Flue Gas Desulfurization (FGD): A Critical Review. *Environ. Sci. Pollut. Res.* **2023**, *30*, 76471–76490. [CrossRef]
16. Ning, H.; Tang, R.; Li, C.; Gu, X.; Gong, Z.; Zhu, C.; Li, J.; Wang, K.; Yu, J. Recent Advances in Process and Materials for Dry Desulfurization of Industrial Flue Gas: An Overview. *Sep. Purif. Technol.* **2025**, *353*, 128425. [CrossRef]
17. Hanif, M.A.; Ibrahim, N.; Abdul Jalil, A. Sulfur Dioxide Removal: An Overview of Regenerative Flue Gas Desulfurization and Factors Affecting Desulfurization Capacity and Sorbent Regeneration. *Environ. Sci. Pollut. Res.* **2020**, *27*, 27515–27540. [CrossRef]
18. Luo, L.; Guo, Y.; Zhu, T.; Zheng, Y. Adsorption Species Distribution and Multicomponent Adsorption Mechanism of SO_2, NO, and CO_2 on Commercial Adsorbents. *Energy Fuels* **2017**, *31*, 11026–11033. [CrossRef]

19. Yang, K.; Su, B.; Shi, L.; Wang, H.; Cui, Q. Adsorption Mechanism and Regeneration Performance of 13X for H_2S and SO_2. *Energy Fuels* **2018**, *32*, 12742–12749. [CrossRef]

20. COMSOL Multiphysics® v. 6.2. COMSOL AB, Stockholm, Sweden. Available online: www.comsol.com (accessed on 15 September 2024).

21. Bourgeois, S.V.; Groves, F.R.; Wehe, A.H. Analysis of Fixed Bed Sorption: Flue Gas Desulfurization. *AIChE J.* **1974**, *20*, 94–103. [CrossRef]

22. Hu, Q.; Xie, Y.; Zhang, Z. Modification of Breakthrough Models in a Continuous-Flow Fixed-Bed Column: Mathematical Characteristics of Breakthrough Curves and Rate Profiles. *Sep. Purif. Technol.* **2020**, *238*, 116399. [CrossRef]

23. Thomas, H.C. Heterogeneous Ion Exchange in a Flowing System. *J. Am. Chem. Soc.* **1944**, *66*, 1664–1666. [CrossRef]

24. Boonchuay, A.; Worathanakul, P. The Diffusion Behavior of CO_2 Adsorption from a CO_2/N_2 Gas Mixture on Zeolite 5A in a Fixed-Bed Column. *Atmosphere* **2022**, *13*, 513. [CrossRef]

25. Rojas-Mayorga, C.K.; Aguayo-Villarreal, I.A.; Moreno-Pérez, J.; Muñiz-Valencia, R.; Montes-Morán, M.Á.; Ocampo-Pérez, R. Influence of Calcium Species on SO_2 Adsorption Capacity of a Novel Carbonaceous Materials and Their ANN Modeling. *J. Environ. Chem. Eng.* **2021**, *9*, 104810. [CrossRef]

26. Makrigianni, V.; Giannakas, A.; Hela, D.; Papadaki, M.; Konstantinou, I. Adsorption of Methylene Blue Dye by Pyrolytic Tire Char in Fixed-Bed Column. *Desalin. Water Treat.* **2017**, *65*, 346–358. [CrossRef]

27. Guzzinati, R.; Sarti, E.; Catani, M.; Costa, V.; Pagnoni, A.; Martucci, A.; Rodeghero, E.; Capitani, D.; Pietrantonio, M.; Cavazzini, A.; et al. Formation of Supramolecular Clusters at the Interface of Zeolite X Following the Adsorption of Rare-Earth Cations and Their Impact on the Macroscopic Properties of the Zeolite. *ChemPhysChem* **2018**, *19*, 2208–2217. [CrossRef]

28. Speranza, G.; Canteri, R. RxpsG a New Open Project for Photoelectron and Electron Spectroscopy Data Processing. *SoftwareX* **2019**, *10*, 100282. [CrossRef]

29. Hamid, A.; Wilson, A.E.; Torbert, H.A.; Wang, D. Sorptive Removal of Phosphorus by Flue Gas Desulfurization Gypsum in Batch and Column Systems. *Chemosphere* **2023**, *320*, 138062. [CrossRef]

30. Garea, A.; Herrera, J.L.; Marques, J.A.; Irabien, A. Kinetics of Dry Flue Gas Desulfurization at Low Temperatures Using $Ca(OH)_2$: Competitive Reactions of Sulfation and Carbonation. *Chem. Eng. Sci.* **2001**, *56*, 1387–1393. [CrossRef]

31. Lǚ, J.; Fu, Y.; Yu, H.; Wang, H.; Wang, Z.; Chen, H. Effect of Relative Humidity on the Desulfurization Performance of Calcium-Based Desulfurizer. *J. Environ. Sci.* **2024**, *138*, 179–188. [CrossRef]

32. Li, C.H.; Wang, H.; Hu, J.H.; Wu, Z.F. Study of Desulphurization Using CaO Powder Trengthened by Fe_2O_3 at Medium Temperature. *Appl. Chem. Ind.* **2006**, *2*, 92–95. [CrossRef]

33. Zheng, X.R.; Liang, Y.B.; Tan, Y.Y. Effect of High-Content Iron Ash on Removal of SO_2 by Calcium-Based Desulfurizer. *J. China Coal Soc.* **2021**, *47*, 350–355. [CrossRef]

34. García-Martínez, J.; Bueno-López, A.; García-García, A.; Linares-Solano, A. SO_2 Retention at Low Temperatures by $Ca(OH)_2$-Derived CaO: A Model for CaO Regeneration. *Fuel* **2002**, *81*, 305–313. [CrossRef]

35. Dahlan, I.; Lee, K.T.; Kamaruddin, A.H.; Mohamed, A.R. Evaluation of Various Additives on the Preparation of Rice Husk Ash (RHA)/CaO-Based Sorbent for Flue Gas Desulfurization (FGD) at Low Temperature. *J. Hazard. Mater.* **2009**, *161*, 570–574. [CrossRef] [PubMed]

36. Li, G.; Wang, Q.; Jiang, T.; Luo, J.; Rao, M.; Peng, Z. Roll-up Effect of Sulfur Dioxide Adsorption on Zeolites FAU 13X and LTA 5A. *Adsorption* **2017**, *23*, 699–710. [CrossRef]

37. Deng, H.; Yi, H.; Tang, X.; Liu, H.; Zhou, X. Interactive Effect for Simultaneous Removal of SO_2, NO, and CO_2 in Flue Gas on Ion Exchanged Zeolites. *Ind. Eng. Chem. Res.* **2013**, *52*, 6778–6784. [CrossRef]

38. Mahmoodi Meimand, M.; Javid, N.; Malakootian, M. Adsorption of Sulfur Dioxide on Clinoptilolite/Nano Iron Oxide and Natural Clinoptilolite. *Health Scope* **2019**, *in press*. [CrossRef]

39. Pedrolo, D.R.S.; de Menezes Quines, L.K.; de Souza, G.; Marcilio, N.R. Synthesis of Zeolites from Brazilian Coal Ash and Its Application in SO_2 Adsorption. *J. Environ. Chem. Eng.* **2017**, *5*, 4788–4794. [CrossRef]

40. Alarcon-Ruiz, L.; Platret, G.; Massieu, E.; Ehrlacher, A. The Use of Thermal Analysis in Assessing the Effect of Temperature on a Cement Paste. *Cem. Concr. Res.* **2005**, *35*, 609–613. [CrossRef]

41. Villagrán-Zaccardi, Y.A.; Egüez-Alava, H.; De Buysser, K.; Gruyaert, E.; De Belie, N. Calibrated Quantitative Thermogravimetric Analysis for the Determination of Portlandite and Calcite Content in Hydrated Cementitious Systems. *Mater. Struct.* **2017**, *50*, 179. [CrossRef]

42. Baltrusaitis, J.; Usher, C.R.; Grassian, V.H. Reactions of Sulfur Dioxide on Calcium Carbonate Single Crystal and Particle Surfaces at the Adsorbed Water Carbonate Interface. *Phys. Chem. Chem. Phys.* **2007**, *9*, 3011. [CrossRef]

43. Luque, A.; Martínez de Yuso, M.V.; Cultrone, G.; Sebastián, E. Analysis of the Surface of Different Marbles by X-Ray Photoelectron Spectroscopy (XPS) to Evaluate Decay by SO_2 Attack. *Environ. Earth Sci.* **2013**, *68*, 833–845. [CrossRef]

44. Zewdie, D.T.; Bizualem, Y.D.; Nurie, A.G. A Review on Removal CO_2, SO_2, and H_2S from Flue Gases Using Zeolite Based Adsorbents. *Discov. Appl. Sci.* **2024**, *6*, 331. [CrossRef]

45. Roque-Malherbe, R. Complementary Approach to the Volume Filling Theory of Adsorption in Zeolites. *Microporous Mesoporous Mater.* **2000**, *41*, 227–240. [CrossRef]

46. Emelianova, A.; Balzer, C.; Reichenauer, G.; Gor, G.Y. Adsorption-Induced Deformation of Zeolites 4A and 13X: Experimental and Molecular Simulation Study. *Langmuir* **2023**, *39*, 11388–11397. [CrossRef] [PubMed]

47. Gor, G.Y.; Huber, P.; Bernstein, N. Adsorption-Induced Deformation of Nanoporous Materials—A Review. *Appl. Phys. Rev.* **2017**, *4*, 011303. [CrossRef]

48. Nasluzov, V.A.; Shor, A.M.; Nörtemann, F.; Staufer, M.; Yudanov, I.V.; Rösch, N. Density Functional Study of SO_2 Adsorption in HY Zeolites. *J. Mol. Struct. Theochem.* **1999**, *466*, 235–244. [CrossRef]

49. Kolle, J.M.; Fayaz, M.; Sayari, A. Understanding the Effect of Water on CO_2 Adsorption. *Chem. Rev.* **2021**, *121*, 7280–7345. [CrossRef]

50. Boer, D.G.; Langerak, J.; Pescarmona, P.P. Zeolites as Selective Adsorbents for CO_2 Separation. *ACS Appl. Energy Mater.* **2023**, *6*, 2634–2656. [CrossRef]

51. Choeichom, P.; Sirivat, A. Discriminative Sensing Performances of ZSM-5, Y, Mordenite, Ferrierite, Beta, 3A, 4A, 5A, and 13X Zeolites Towards Sulfur Dioxide. *Ionics* **2018**, *24*, 2829–2841. [CrossRef]

52. Kirschhock, C.E.A.; Sultana, A.; Godard, E.; Martens, J.A. Adsorption Chemistry of Sulfur Dioxide in Hydrated Na–Y Zeolite. *Angew. Chem. Int. Ed.* **2004**, *43*, 3722–3724. [CrossRef]